Selective laser melting of Zr-based bulk metallic glasses: Processing, microstructure and mechanical properties

X.P. Li [a,b,*], M.P. Roberts [c], S. O'Keeffe [d], T.B. Sercombe [a,**]

[a] The University of Western Australia, School of Mechanical and Chemical Engineering, Perth, WA 6009, Australia
[b] University of Leuven (KU Leuven), Department of Mechanical Engineering, 3001 Leuven, Belgium
[c] The University of Western Australia, Centre for Microscopy, Characterisation and Analysis, Perth, WA 6009, Australia
[d] Liquidmetal Technologies Inc., 30452 Esperanza, Rancho Santa Margarita, CA 92688, USA

HIGHLIGHTS

- Large scale, complex and fully dense crack-free Zr-based BMGs can be achieved using SLM.
- The fabricated BMGs have high hardness, high compressive strength and a small amount of ductility.
- The phase formation, microstructure and mechanical properties of the BMGs can be tailored by controlling SLM parameters.
- Chemical homogeneity within the melt pool plays a critical role in determining the amorphous nature of the fabricated BMGs.
- Multiple scans can result in an averaging of the melt pool and therefore benefit the formation of amorphous phase.

GRAPHICAL ABSTRACT
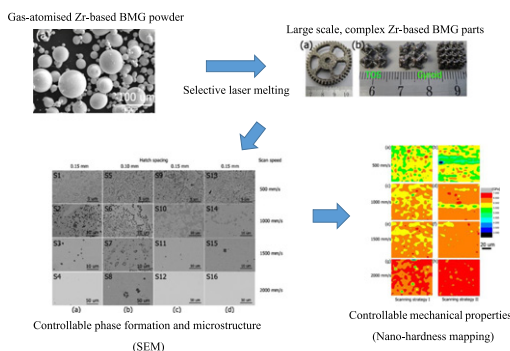
ARTICLE INFO

ABSTRACT

This study shows that large scale, complex and fully dense crack-free Zr-based bulk metallic glasses (BMGs) with high hardness, high compressive strength and a small amount of ductility can be achieved using selective laser melting (SLM). The results show that higher laser energy density leads to severe crystallisation while lower laser energy density tends to result in the formation of a fully amorphous material. By investigating the chemical distribution of the melt pool, the underlying reason for this behaviour was attributed to the chemical inhomogeneity caused by the melt flow triggered elemental segregation at high energy densities. In addition, the chemical homogeneity can be improved in some cases through the use of a multiple pass scanning strategy. The underlying mechanism is that multiple scans can result in an averaging of the melt flow within the melt pool and therefore a more homogenous distribution of the elements. More importantly, the phase formation, microstructure and mechanical properties of the SLM-fabricated Zr-based BMGs can be effectively tailored by controlling the SLM processing parameters. This provides a novel and promising route to the fabrication of large scale BMGs with complex geometry and desirable mechanical properties.

© 2016 Elsevier Ltd. All rights reserved.

---

* Correspondence to: X.P. Li, The University of Western Australia, School of Mechanical and Chemical Engineering, Perth, WA 6009, Australia.
** Corresponding author.
E-mail addresses: xiaopeng.li@uwa.edu.au, xiaopeng.li@kuleuven.be (X.P. Li), tim.sercombe@uwa.edu.au (T.B. Sercombe).

1. Introduction

From a "pie in the sky" past to a prosperous today, bulk metallic glasses (BMGs), which are characterised by their amorphous microstructure, have enjoyed a rapid development driven by the appreciation of their unique mechanical and functional properties [1–4]. This rapid proliferation of BMGs in the past decades has also extended their applications to a wide spectrum of industries including medical devices, sporting goods, electronic casings, and sensors. [5–9].

Recent progress in the design and fabrication of BMGs has been made to address their main limitation: namely the size and geometry constraints as well as the room temperature macroscopic brittleness in unconstrained conditions [3]. For example, by improving the glass forming ability (GFA) of BMGs through alloy design, parts with a diameter larger than 10 mm have been produced using conventional rapid casting in several alloy systems, e.g. Pd-, La-, Zr- and etc. [3]. However, these BMGs are limited to certain glass forming alloys and always contain five or more elements, which often include high-cost and toxic elements. This makes them prohibitively expensive for most applications.

BMGs with relatively complex geometries can also be fabricated by taking advantage of the considerable softening phenomenon within their supercooled liquid region (SCLR). Known as thermoplastic forming (TPF), these processing techniques include blow molding, hot forming, hot rolling, micro-imprinting, and miniature fabrication [10]. However, TPF requires BMGs with a large SCLR and a high thermal stability, which rules out a large number of important glass forming alloys, especially those marginal BMGs. BMG composites with improved ductility and fracture toughness have also been achieved by introducing a soft second phase into the amorphous matrix either in situ or ex situ [11–14]. However, introducing a second phase is not straightforward when using conventional approaches. In order to form desired microstructure, the glass forming alloys must be highly processable and the cooling rates need to be well controlled. Most importantly, especially when fabricating BMGs composites with large cross-section areas, the inevitable temperature gradient occurring during the fabrication process becomes a serious limitation which prevents the formation of the desired microstructure.

The development of additive manufacturing techniques, especially selective laser melting (SLM), provides a promising alternative to overcome the aforementioned critical issues in the BMGs field [15–17]. Selective laser melting fabricates computer aided design (CAD) components in a layer-wise manner by selectively melting deposited powders [18]. It is characterised by its fully melting process, which distinguishes itself from other known additive manufacturing techniques [18]. SLM has many advantages compared to conventional manufacturing approaches such as the ability to fabricate components with complex geometries and high material usage efficiency [18]. Due to the tiny interaction volume (a few hundred microns) and short interaction time (milliseconds) between the laser beam and the material during SLM, it creates very high heating and cooling rates (10^3–10^8 K/s) [19]. The microstructure can therefore be theoretically tailored at any point within the part by controlling the influential processing parameters such as laser energy, scan speeds, hatch spacing, layer thickness and lens focus offset. All of these render SLM a promising approach to the fabrication of BMGs.

Recently, a few pioneering studies on SLM of BMGs have been reported [15,20,21]. A partially Fe-based BMG scaffold has been produced from metallic glass powder, for the first time demonstrating the feasibility of fabrication BMGs with complex geometries by SLM [15]. However, the density of the scaffold was low and cracking was present. Our recent study using single track scans on already-fabricated porous Al-based BMG shows that fully amorphous microstructure can be achieved by SLM through controlling the processing parameters [21]. The formation of cracks and pores can also be well controlled. Another study also proposed a low-energy re-scan strategy to produce crack-free Al-based BMG composites components with complex geometry, suggesting that

the harmful residual stresses can be partially released by varying the scanning strategy during SLM [20]. However, these studies mainly focused on the concept validation of the fabrication of BMGs via SLM regarding to retaining the amorphous microstructure, achieving complex geometry or preventing cracks. To the best knowledge of the authors, no studies have been reported on the controlling of phase formation and microstructure of BMGs fabricated by SLM and the subsequent influences on the mechanical properties of the fabricated BMG components.

In this work, a systematic study was conducted on the fabrication of a Zr-based BMG via SLM. The influence of the processing parameters on the formation and distribution of the crystalline phases and the final microstructure of the BMG components were investigated in detail. The underlying mechanism for the formation of the microstructure was also discussed and a relation between processing parameters and microstructure was provided. The mechanical properties of the fabricated Zr-based BMGs were also determined. Excellent mechanical properties including high hardness, high strength and a small amount of ductility was shown to be able to be obtained. This work shows that SLM is a promising approach to produce fully dense crack-free BMGs or BMGs composites with complex geometry, large size, controllable microstructure and mechanical properties.

2. Experimental procedures

2.1. Gas-atomisation and selective laser melting (SLM)

Master ingot with a nominal composition of $Zr_{52.5}Ti_5Cu_{17.9}Ni_{14.6}Al_{10}$ (in at.%) was supplied by Liquidmetal® Technologies, Inc. under the trade name LM105. The powder used was produced using electrode induction melting gas atomization (EIGA) and was below 106 μm in diameter ($D_{10} = 30$ μm, $D_{50} = 61$ μm and $D_{90} = 108$ μm), which was obtained through sieving the as-atomised powder.

SLM experiments were conducted using a ReaLizer SLM-100 machine (ReaLizer GmbH, Germany) which was equipped with a fibre laser, generating a laser beam with a wavelength of 1060 nm and maximum power of 200 W at the part bed. A high purity argon gas was used during the processing to minimise oxidation. Because the powder used in this study was sieved at 106 μm, the layer thickness was set to 100 μm. Based on our previous work on the SLM of an Al-based metallic glass (MG) [22], the substrate temperature was set at 200 °C. The laser power was set at 200 W. To investigate the influence of scanning speed, hatch spacing and scanning strategy on the microstructure and mechanical properties of the SLM-fabricated $Zr_{52.5}Ti_5Cu_{17.9}Ni_{14.6}Al_{10}$ bulk metallic glasses (BMGs), four scanning speeds, two hatch spacings and three scanning strategies were used. The details of the processing parameters and the scanning strategies used are listed in Table 1 and Fig. 1, respectively.

2.2. Microstructure and mechanical properties characterisation

The phase formation and microstructure of the SLM-fabricated $Zr_{52.5}Ti_5Cu_{17.9}Ni_{14.6}Al_{10}$ BMGs with different processing parameters were characterised using a FEI Verios 460 scanning electron microscope (SEM, acceleration voltage 15 kV, working distance 6 mm) and X-ray diffraction (XRD, PANalytical Empyrean, D/max III, Cu Kα target, operated at 40 kV and 40 mA with a step size of 0.02° and scanning speed of 2°/min, all the XRD scans were done on the X-Z plane of the sample and therefore representative of the whole sample). Electron probe microanalyser (EPMA, JEOL 8530F microprobe, equipped with 5 tuneable wavelength dispersive spectrometers operated at a 40° take-off angle, a beam energy of 20 keV, beam current of 20 nA for X-ray intensity calibration, and 50 nA for mapping with a dwell time of 100 ms per pixel) was used to characterise the distribution of the constituent elements (Zr, Cu, Ni, Al and Ti) in the SLM-fabricated BMGs.

Table 1
Summary of the SLM parameters and scanning strategies used in this study.

Scanning strategy		Sample	Scan speed, V (mm/s)	Hatch spacing, H (mm)	Laser energy density, E_p (J/mm³)
I	X or Y, once	S1	500	0.15	53.3
		S2	1000	0.15	26.7
		S3	1500	0.15	17.8
		S4	2000	0.15	13.3
		S5	500	0.10	80
		S6	1000	0.10	40
		S7	1500	0.10	26.7
		S8	2000	0.10	20
II	X and Y, once	S9	500	0.15	53.3
		S10	1000	0.15	26.7
		S11	1500	0.15	17.8
		S12	2000	0.15	13.3
III	X and Y, twice	S13	500	0.15	53.3
		S14	1000	0.15	26.7
		S15	1500	0.15	17.8
		S16	2000	0.15	13.3

Hardness mapping (a 100×100 μm area) on the cross-sections of the SLM-fabricated Zr-based BMGs with different processing parameters was obtained using nanoindentation at an indentation load of 2 mN at a rate of 200 μN/s for both loading and unloading (Hysitron® Triboindenter) with a Berkovich indenter of a tip radius of 100 nm. The maximum indentation force applied was 2 mN at a rate of 200 μN/s for both loading and unloading. The dwell time at the peak load was fixed at 10 s. A minimum of 400 indentations were conducted on each area. Compression tests were carried out on SLM-fabricated Zr-based BMG cylinders with a diameter of 3 mm and height 6 mm, using an Instron 5982 machine at a constant strain rate of 1×10^{-4} s^{-1}. At least four samples were tested for each processing condition.

3. Results

3.1. Gas-atomisation and SLM process

As shown in Fig. 2a, the as-fabricated $Zr_{52.5}Ti_5Cu_{17.9}Ni_{14.6}Al_{10}$ MG powders with a diameter from a few microns to ~150 μm are spherical, a typical morphology of the gas-atomisation process. The surface of the powder is smooth, which together with its spherical morphology results in good flowability of the powder, an important requirement during SLM. The cross-section of the powder is shown in Fig. 2b. It is clear that the powder shows a homogenous and featureless microstructure, indicative of its amorphous nature. The XRD patterns of the as-fabricated powder and the sieved (~106 μm) powder are shown in Fig. 2c. Both cases show a broad halo peak without any apparent crystalline peaks being detected, again indicating their amorphous nature.

In order to investigate the phase formation, microstructure and mechanical properties of the fabricated BMGs, cubes ($10 \times 10 \times 5$ mm) and cylinders (3×6 mm, diameter by height) were made with different processing parameters (see Table 1). A selection of the as-built parts is shown in Fig. 3. The surface finish of the cubes and cylinders varied with different SLM parameters. Lower laser energy density ($\overline{E_p}$, in this

study $\overline{E_p} \sim \frac{P}{V \cdot h \cdot t}$ where P is the laser power, h is the hatch spacing, t is the layer thickness, V is the laser scan speed [23]) resulted in a shiny but rough sample surface while higher $\overline{E_p}$ led to a darker, smooth surface. However, the sample surface became much smoother when introducing scan strategies II and III.

3.2. Phase formation and microstructure

The XRD patterns for samples S1–S4 fabricated using different scan speeds are shown in Fig. 4. For S1, only sharp crystalline peaks can be observed, suggesting that the fabricated samples were fully crystallised. For S2, some sharp crystalline peaks overlap with a broad halo peak, which implies that the sample was partially crystallised. For S3, the crystalline peaks become weaker while a broad halo peak becomes more dominant, suggesting a higher volume fraction of the amorphous phase. Using condition S4, only a broad halo peak can be observed without any crystalline peaks, indicative of the essentially amorphous nature of the sample. The corresponding back-scattered electron (BSE) SEM images of the cross-sections of the fabricated samples S1–S4 are shown in Fig. 5a. It can be seen that sample S1 was fully crystallised with the formation of randomly distributed coarse (~0.5 μm) and fine (~100 nm) crystals. In S2, some dark uniaxial crystals with a diameter mostly below 1 μm can be seen embedded in a featureless amorphous matrix. Although the number of crystals decreased in S3, they became larger, ~2 μm. In S4, no crystals can be seen and the whole sample exhibited a homogeneous and featureless microstructure, again indicative of its amorphous nature. This demonstrates that SLM is capable of fabricating large size fully amorphous BMGs. Unlike S1 and S2, a few small pores can be observed in S3 and S4, probably caused by the insufficient densification at low $\overline{E_p}$.

The BSE images of the cross-sections of the samples S5–S8 fabricated using 0.10 hatch spacing are shown in Fig. 5b. Using the smaller hatch spacing of S5–S7 resulted in the crystallisation becoming more severe, with large crystals forming. This was probably due to the higher $\overline{E_p}$ delivered to the powder. In S8, the samples were also partially crystallised with some crystals being observed. However, no pores can be seen, suggesting that the laser energy at 0.10 mm hatch spacing and 2000 mm/s scan speed was sufficient to densify the Zr-based MG powder.

Fig. 5c and d show the microstructure of the samples S9–S16 fabricated using scan strategies II and III (i.e. scanning twice and four times), respectively. It can be seen that S9 and S13 had larger crystals in comparison to S1 fabricated using the scanning strategy I. Unlike the random distribution of the crystals in S1, the crystals in S9 and S13 formed in bands across the samples where these crystals were all large and elongated. Interestingly, in S10 and S14, fewer crystals formed compared to the scanning strategy I (i.e. sample S2). This implies that scanning multiple times during SLM facilitated the formation of the amorphous phase provided that the energy was not too high. However multiple scanning caused coarsening of the crystals, which is especially evident in S15. In S12 and S16, there was no significant microstructural difference caused by the different scanning strategies. The samples still showed a homogenous and featureless microstructure.
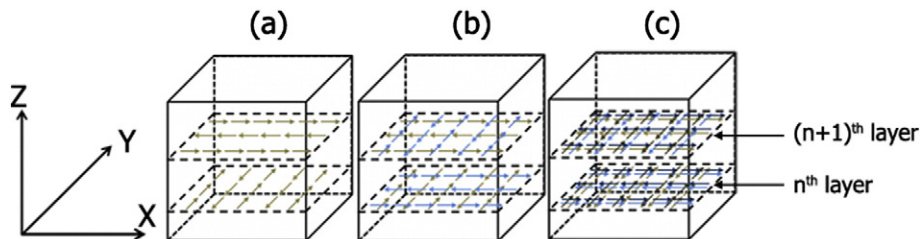

Fig. 1. A schematic illustration showing the three scanning strategies used in this study: (a) X or Y, once; (b) X and Y, once and (c) X and Y, twice.
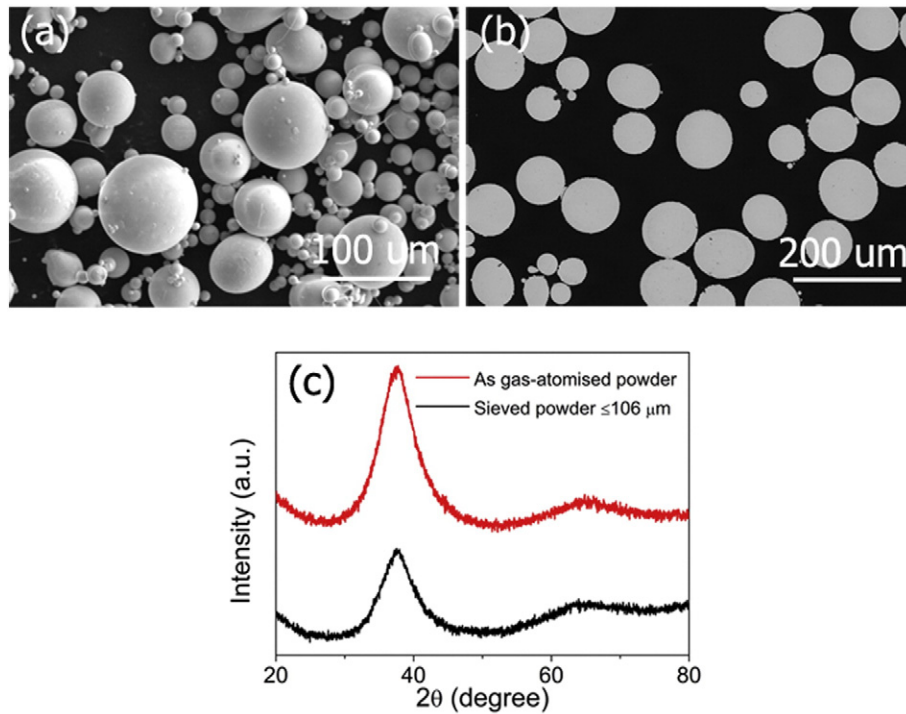
Fig. 2. (a) A secondary electron SEM image showing the spherical morphology of the as gas-atomised $Zr_{52.5}Ti_5Cu_{17.9}Ni_{14.6}Al_{10}$ MG powder; (b) a back-scattered SEM image of the powder; (c) XRD patterns of the as gas-atomised and sieved powder.

The influence of the scanning strategy on the microstructure of the samples can also be observed in the XRD patterns shown in Fig. 6. It is clear that at scan speeds of both 500 and 2000 mm/s, there the scanning strategy had no effect on the resultant structure. However, at scan speeds of 1000 and 1500 mm/s, the XRD patterns clearly show that the sharp crystalline peaks weaken on multiple scanning (in comparison to Fig. 4), suggesting that more amorphous phase was formed. This further implies that multiple scanning can turn the already-formed crystalline phases within the samples into amorphous phases.

3.3. Mechanical properties

Fig. 7 shows the nano-hardness maps of the samples S1–S4 and S13–S16 (i.e. scanning strategy I and III). When using the scanning strategy I, the hardness of the fabricated BMGs increased upon increasing the scan speeds. In S1, the average hardness was ~5.5 GPa. In S4, the average hardness reached ~6.5 GPa. Only a slight increase in hardness can be detected from S2 to S3, which had a value ~6.0 GPa. In addition, as the scan speed increased, the hardness variation decreased and the sample appeared to become more homogenous. Despite being fully amorphous, sample S4 (Fig. 7g) did not have a uniform hardness.

When using the scanning strategy III, a similar trend on increasing hardness scan speed was also observed. It is interesting to note that banding is apparent in S13 and S14 (Fig. 7b and d), which is in
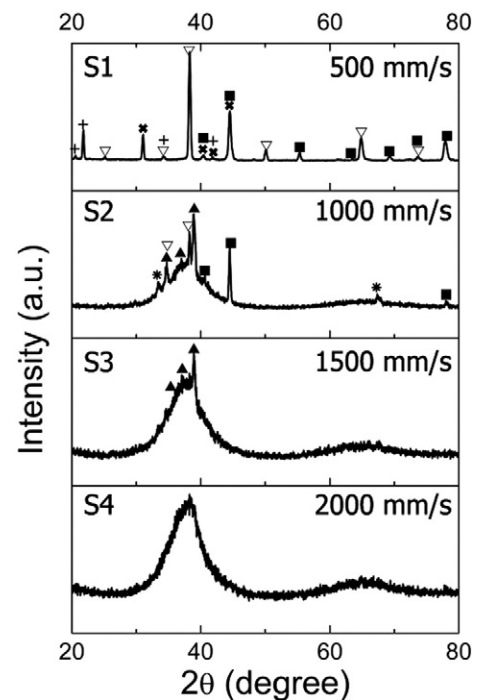

Fig. 3. SLM-fabricated $Zr_{52.5}Ti_5Cu_{17.9}Ni_{14.6}Al_{10}$ BMG cubes (10 × 10 × 5 mm) and cylinders (3 × 6 mm, diameter by height).

Fig. 4. XRD patterns of the SLM-fabricated $Zr_{52.5}Ti_5Cu_{17.9}Ni_{14.6}Al_{10}$ BMGs at different scan speeds with the same hatch spacing 0.15 mm and scanning strategy I (▲ NiZr-type phase, ▽ rhombohedral phase, ✖ ZrAl-type phase, ■ monoclinic phase, + AlNiZr-type phase and * unidentified phase). Future work is needed to identify the unidentified phase.
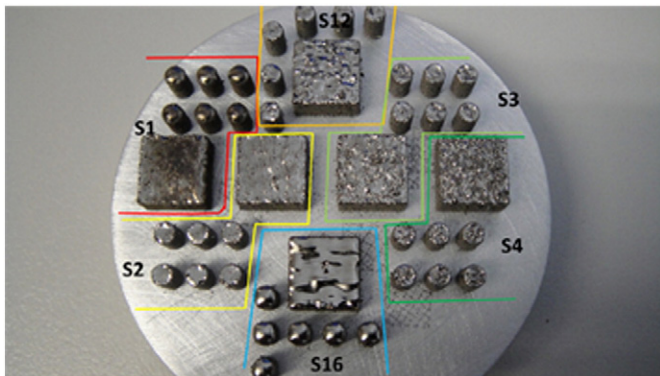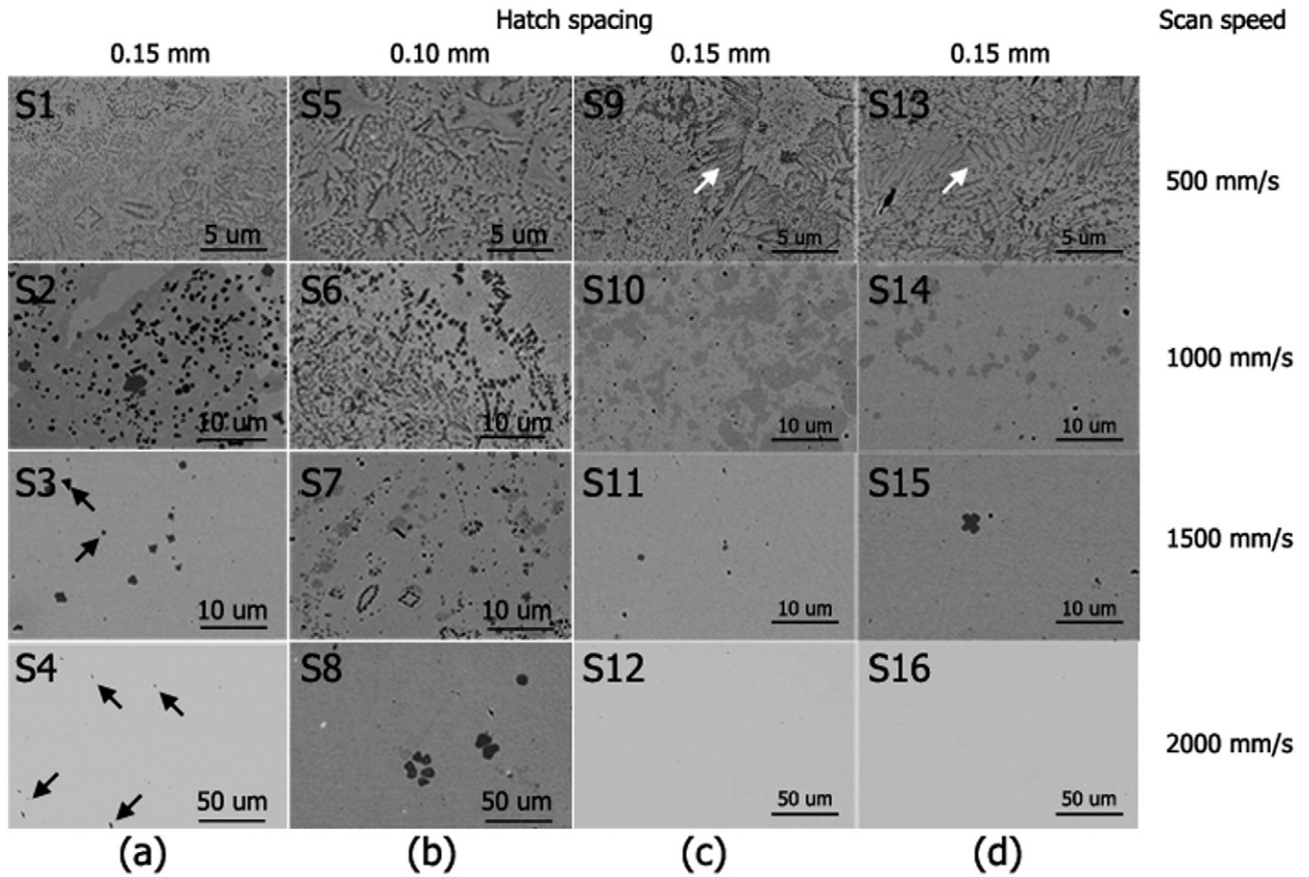
Fig. 5. BSE-SEM images of the SLM-fabricated $Zr_{52.5}Ti_5Cu_{17.9}Ni_{14.6}Al_{10}$ BMGs at different scan speeds, hatch spacings and scanning strategies: (a) S1–S4; (b) S5–S8; (c) S9–S12 and (d) S13–S16. Arrows (in black) point to the pores and arrows (in white) point to the bands.
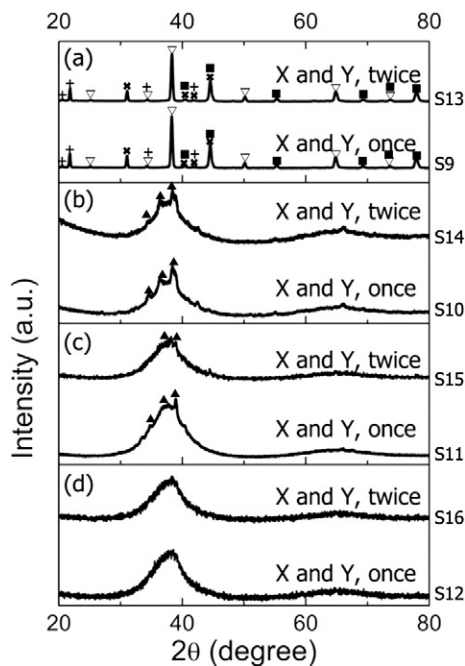

Fig. 6. XRD patterns of the SLM-fabricated $Zr_{52.5}Ti_5Cu_{17.9}Ni_{14.6}Al_{10}$ BMGs at different scan speeds (mm/s): (a) 500; (b) 1000; (c) 1500 and (d) 2000 with scanning strategies II and III. (▲ NiZr-type phase, ▽ rhombohedral phase, ✖ ZrAl-type phase, ■ monoclinic phase, + AlNiZr-type phase and * unidentified phase).

consistent with the microstructural observations in Fig. 5. When compared to the scanning strategy I, multiple scans increased both the average hardness and the uniformity of the hardness distribution. This was especially true at the faster scan speeds.

The compressive strength of the BMGs (S1–S4, S9–S16) fabricated with different scan speeds and scanning strategies is shown in Fig. 8a. The highest compressive strength was achieved in samples fabricated at 1500 and 2000 mm/s with a value ~1.5 GPa. At these scan speeds, the scanning strategy had little influence on the compressive strength. In contrast, the sample fabricated at 500 mm/s had the lowest compressive strength ~0.6 GPa and its strength decreased with increasing scan times. For samples fabricated at 1000 mm/s, the compressive strength increased with the number of scans. Typical stress-strain curves for the samples S1–S4 are shown in Fig. 8b. The samples S1, S2 and S4 show no ductility while S3 exhibited a very small amount of apparent ductility (~0.5%).

Some large scale and complex geometry structures including a sample gear with a diameter of ~35 mm and height 5 mm and a 15% solid fraction topology optimised structure (TOS) [24] and two Gyroid structures with 5 mm and 2.5 mm unit cells were successfully fabricated via SLM of the $Zr_{52.5}Ti_5Cu_{17.9}Ni_{14.6}Al_{10}$ MG powder, as shown in Fig. 9a and b, respectively. No cracks, apparent pores or distortion can be seen, indicating that the capability of SLM in processing $Zr_{52.5}Ti_5Cu_{17.9}Ni_{14.6}Al_{10}$ MG.

4. Discussion

4.1. The influence of scan speed on phase formation and microstructure

SLM is characterised by very rapid cooling of the melt pool (cooling rates ~10^3 to 10^8 °C/s) [19]. According to our previous study on the SLM
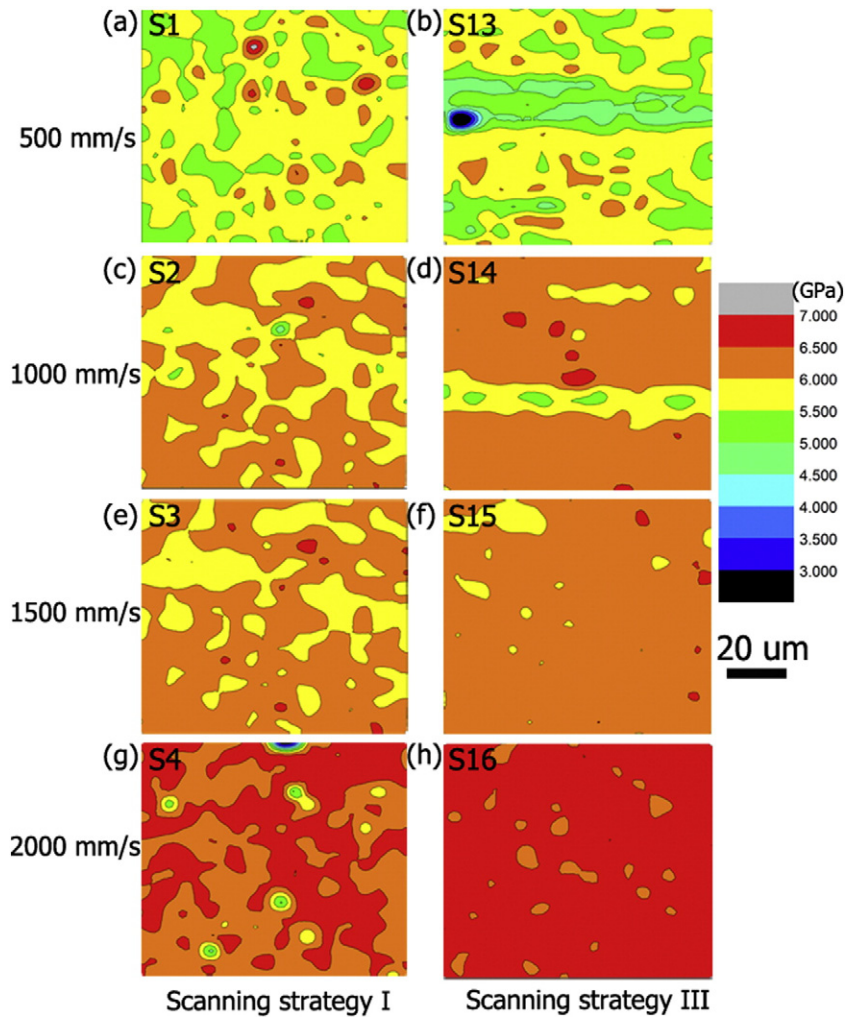
Fig. 7. Nano-hardness mapping of the SLM-fabricated $Zr_{52.5}Ti_5Cu_{17.9}Ni_{14.6}Al_{10}$ BMGs at different scan speeds (mm/s): (a) and (b) 500; (c) and (d) 1000; (e) and (f) 1500 and (g) and (h) 2000 and different scanning strategies: (a), (c), (e) and (g) scanning strategy I and (b), (d), (f) and (h) scanning strategy III.

of a marginal Al-based ($Al_{86}Ni_6Y_{4.5}Co_2La_{1.5}$, in at.%) MG [22], the cooling rate is dependent on the laser scan speed and a minimum value ~10^3 °C/s can be achieved at a laser scan speed of 2000 mm/s. Although the cooling rate during SLM depends on many factors such as SLM processing parameters and the composition of the materials [25], the high cooling rate during SLM is mainly caused by the large temperature difference between the melt pool and substrate. Therefore, the

cooling rate during SLM of $Zr_{52.5}Ti_5Cu_{17.9}Ni_{14.6}Al_{10}$ when using the same scan speed of 2000 mm/s can be estimated to have a value with a magnitude of ~10^3 °C/s. This is much higher than the critical cooling rate R_c of this Zr-based BMG (~10^2 °C/s) [3]. From this aspect, it appears reasonable that a fully amorphous $Zr_{52.5}Ti_5Cu_{17.9}Ni_{14.6}Al_{10}$ BMG was obtained at a scan speed 2000 mm/s (Figs. 4 and 5). During SLM, increasing $\overline{E_p}$ results in a higher cooling rate [26] and therefore it was expected that
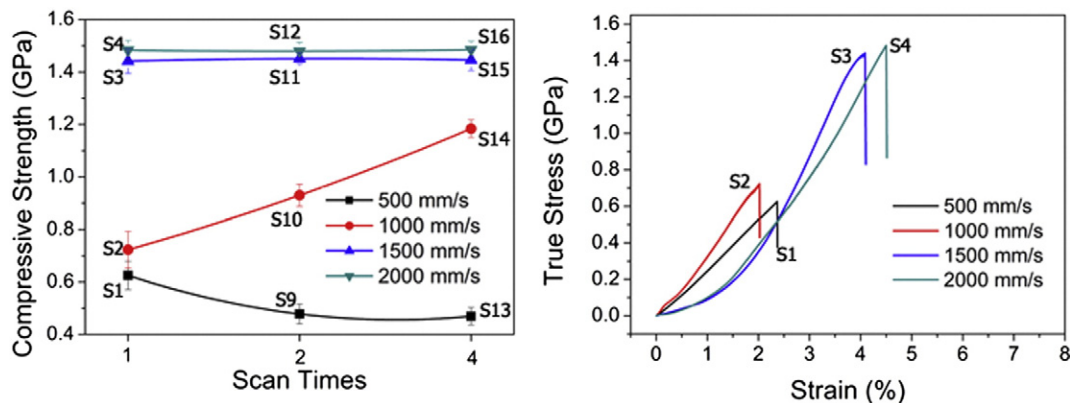

Fig. 8. (a) Compressive strength of the SLM-fabricated $Zr_{52.5}Ti_5Cu_{17.9}Ni_{14.6}Al_{10}$ BMGs at different scan speeds and different scanning strategies; (b) typical stress-strain curves of the parts fabricated at different scan speeds using scanning strategy I.
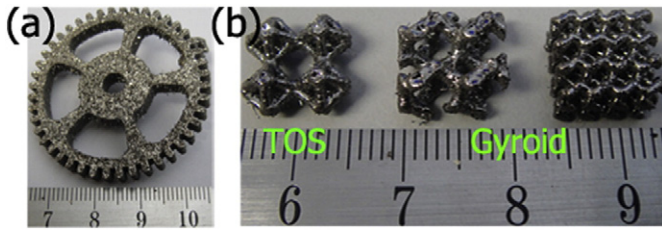
Fig. 9. SLM-fabricated $Zr_{52.5}Ti_5Cu_{17.9}Ni_{14.6}Al_{10}$ BMG parts: (a) a sample gear (diameter ~ 35 mm and height 5 mm); (b) a topology optimised structure (TOS) and two Gyroid structures with 5 mm and 2.5 mm unit cells.

the $Zr_{52.5}Ti_5Cu_{17.9}Ni_{14.6}Al_{10}$ MGs fabricated at higher $\overline{E_p}$ should also be amorphous. However, the results show an opposite effect – that is high laser energy densities led to crystallisation (Figs. 4 and 5). This result is also consistent with what was found with an Al-based MG [21] and implies that the formation of the amorphous phase is not solely dependent on the cooling rate.

It has been reported that at least two melt flow patterns are triggered by the laser in the melt pool: damped capillary oscillations and thermocapillary flows [27]. This means that it is possible for the laser to alter the chemical homogeneity (distribution of the constituent elements) of the melt alloy due to the formation of liquid oscillations or capillary waves within the melt pool [28]. According to a previous study [27], thermocapillary flows dominate the damped capillary oscillations when at high $\overline{E_p}$ and a dimensionless number l_n was introduced to quantify the extent of thermocapillary flow as shown below,

$$l_n \sim \frac{\Theta_m \alpha_A \sigma}{\mu c'_v} \bullet \frac{\overline{E_p}\tau}{r_b} \qquad (1)$$

where l_n is the average displacement of a liquid particle divided by the melt pool radius. Θ_m is the normalised temperature, α_A is the laser absorptivity, σ is the surface tension, μ is the dynamic viscosity, c'_v is the volumetric heat capacity, τ is the laser duration time and r_b is the laser beam radius. Given the same material was used in this study, $\frac{\Theta_m \alpha_A \sigma}{\mu c'_v}$ is constant. Hence, l_n is only related to $\frac{\overline{E_p}\tau}{r_b}$, which is only laser parameter related where τ and r_b are constant. Based on this, the higher the $\overline{E_p}$ the stronger the thermocapillary flow (l_n) will be, resulting in a more inhomogeneous melt pool. It is known that glass forming alloys must exhibit chemical homogeneity in order to avoid crystallisation [3]. Therefore, this chemical inhomogeneity caused by the laser-triggered melt flow within the melt pool may be one of the underlying reasons for the observed crystallisation, despite the high cooling rates (Figs. 4 and 5). Characterisation of the chemical homogeneity within the melt pool during SLM is extremely difficult due to the short interaction time (millisecond) and the tiny interaction volume between the laser and the materials. However, the rapid cooling should freeze-in any chemical inhomogeneity and therefore, EMPA was used to characterise the chemical homogeneity of the $Zr_{52.5}Ti_5Cu_{17.9}Ni_{14.6}Al_{10}$ BMGs, as shown in Fig. 10. At higher $\overline{E_p}$, the distribution of the constituent elements (Zr, Cu, Ni, Al and Ti) is inhomogeneous (Fig. 10a). However, with decreasing $\overline{E_p}$, the fluid flow in the melt pool becomes weaker and hence the distribution of the constituent elements became more homogenous (Fig. 10b and c). At the lowest $\overline{E_p}$, a homogeneous distribution of the five constituent elements was obtained (Fig. 10c). This uniform composition then favours the formation of amorphous material during cooling.

4.2. The influence of scanning strategy on phase formation and microstructure

As discussed above, higher $\overline{E_p}$ led to an inhomogeneous chemical distribution, which originated from the liquid flow in the melt pool.

Following this, the scanning strategy III (which scans each layer four times) should increase the melt flow and lead to an even more inhomogeneous chemical distribution. However, as shown in Fig. 11a, at higher $\overline{E_p}$, the distribution of elements becomes more homogeneous compared to the scanning strategy I (single scans - Fig. 10a). The melt flow provides a force which can move the constituent elements within the melt pool. In addition, since the laser beam energy has a Gaussian distribution (TEM_{00}, $M^2 < 1.05$) [26] and the laser beam diameter (~35 μm) is smaller than the point distance (40 to 160 μm) and hatch spacing (0.15 mm), the laser energy would be unevenly distributed across the Zr-based BMG layer. Therefore, using scanning strategy I is likely to induce an unevenly distributed force, causing elemental segregation to occur. This results in a very inhomogeneous and random distribution of the constituent elements (Fig. 10a). In contrast, multiple scans using the scanning strategy III would compensate the abovementioned influence of Gaussian-like distributed laser energy, diameter of the laser beam, point distance and hatch spacing, resulting in an averaging of the melt flow. This averaged melt flow would induce better uniformity of the constituent elements. This is why the distribution of elements becomes more homogenous after multiple scans at higher $\overline{E_p}$ (Fig. 11a). At intermediate $\overline{E_p}$, the distribution of the all the elements also become more homogeneous (Fig. 11b), while at the lowest $\overline{E_p}$, the initial homogenous structure is retained (Fig. 11c). Since a homogeneous melt is one of the important requirements for forming an amorphous structure, scanning multiple times increases the amount of the amorphous phase (Figs. 4 to 6), all but the highest energy density. It should be pointed out that for scanning strategies II and III, the Zr-based BMG samples were solid after the first scan. This facilitated the formation of amorphous phases as a result of the expected higher cooling rate during the subsequent scans after the first scan when compared with scanning strategy I.

4.3. Heat affected zone (HAZ) and oxidation

Due to the existence of an inevitable heat affected zone (HAZ) during SLM, the thermal stability of the BMGs should be high enough to resist devitrification caused by the heat generated by the subsequent layers [18,21]. According to our previous studies on SLM of a marginal Al-based BMG [21], higher $\overline{E_p}$ would lead to a larger HAZ where severe crystallisation occurs. This is consistent with our finding in this study. However, in contrast to our previous study where at lower $\overline{E_p}$ some crystals formed in the HAZ, no crystals were observed at lower $\overline{E_p}$ in this study. The underlying reasons for this are twofold. Firstly, the Zr-based MGs has significantly better glass forming ability (GFA) and thermal stability compared to our previous marginal Al-based MGs [3, 29]. Secondly, the glass transition temperature (T_g) and crystallisation on-set temperature (T_x) of a MG is heating rate-dependent [30]. Above a certain heating rate, so-called critical heating rate (R_h), the crystallisation can be avoided entirely during the heating process [30]. Since the SLM processes is also characterised by a very high heating rate, crystallisation may be avoided. Nonetheless, it is clear that better GFA and high thermal stability are key factors in the fabrication of fully amorphous BMGs via SLM. Furthermore, provided the energy was low, scanning the layer multiple times (i.e. strategy II and III) did not trigger the devitrification process of the Zr-based MGs (Figs. 5 and 11c).

The fabrication process of BMGs must be carried out in either a vacuum or inert atmosphere in order to avoid oxidation [31]. At high $\overline{E_p}$, the melt pool gets hotter and stays hotter for longer compared to lower $\overline{E_p}$, increasing the risk of oxidation. In addition, multiple scanning of the layer will also tend to promote oxidation. However, as can be seen from Figs. 5, 6 and 11b, the samples being scanned multiple times contain more amorphous phase. This implies that oxidation in this study may not be a major factor in determining the formation of amorphous phases.
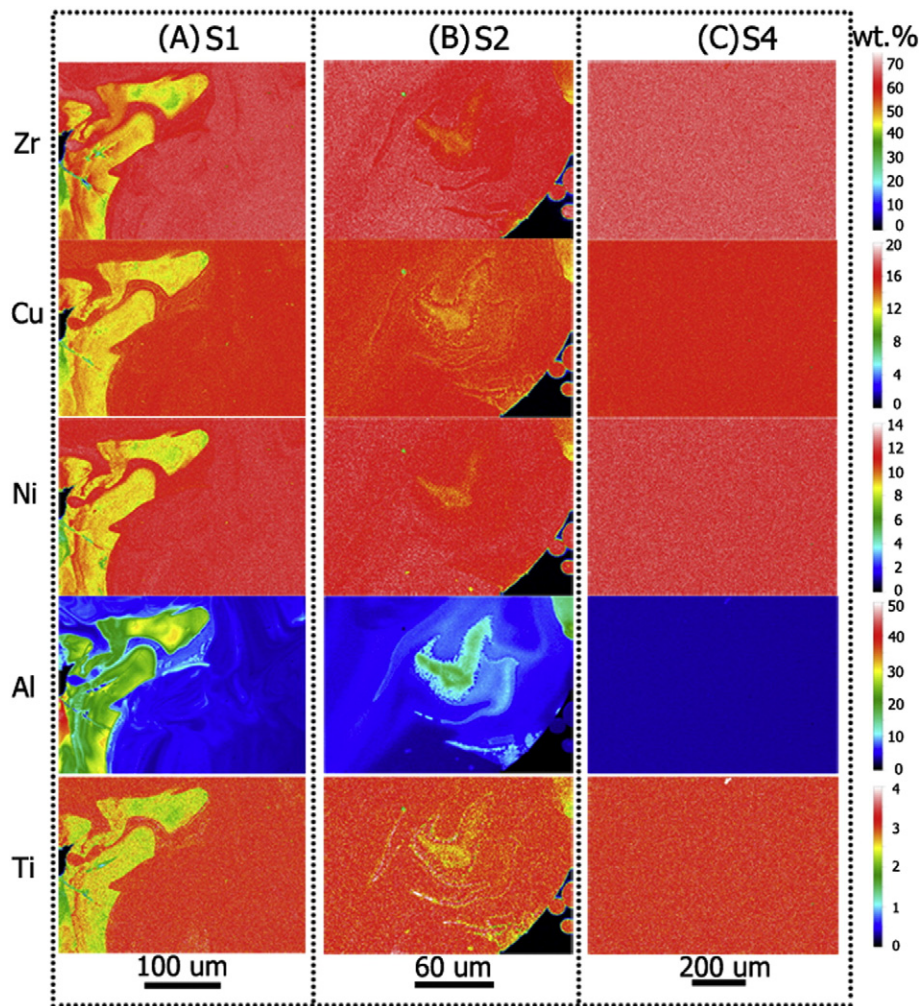
Fig. 10. Quantitative chemical maps obtained using EPMA showing the constituent elements distribution within the SLM-fabricated $Zr_{52.5}Ti_5Cu_{17.9}Ni_{14.6}Al_{10}$ BMGs using scanning strategy I at different scan speeds: (a) 500; (b) 1000 and (c) 2000 mm/s.

4.4. Microstructure control and mechanical properties

It has been reported that SLM of crystalline materials e.g. Al, Ti, Ni alloys and steel can result in the formation of unique microstructures e.g. ultrafine grain size and metastable phases [32–36]. This has been attributed to the characteristics of the manufacturing process; that is the tiny interaction volume and short interaction time between the laser and material which results in very high heating and cooling rates. Theoretically this unique manufacturing process also enables the microstructure to be tailored at any point within the metal components by manipulating the processing parameters. Similarly, as for SLM of MGs, the phase formation, crystallisation and microstructure can also be changed by manipulating the SLM processing parameters, which changes the cooling rate, chemical homogeneity, HAZ, etc. (as discussed in Sections 4.1 and 4.2). The capability to control the microstructure of the SLM-fabricated BMGs further provides a unique and promising route to tailor the mechanical properties of the BMGs. Fully crystallised components give rise to lower compression strength and hardness due to the formation of brittle intermetallics as well as the coarsening and banding of the microstructure. Fully amorphous components have high compression strength and hardness (Figs. 7 and 8) as a result of the amorphous nature [3,9,37]. Between these two extremes, the amount of crystalline phase can be altered by, for example, varying the scanning strategy at a scan speed of 1000 mm/s. This resulted in changes to the compressive strength and hardness of the fabricated samples (Figs. 7 and 8), as a

direct consequence of altering the amount of the amorphous phase. At a scan speed of 2000 mm/s, multiple scans increased the average hardness and uniformity of the hardness distribution of the fabricated BMGs, which was probably caused by the decreasing free volume within the fabricated BMGs [3,9,21,38]. In addition, the fully amorphous Zr-based BMG in this study (e.g. S4) had a higher hardness (~6.5 GPa) and a similar strength (~1.5 GPa) compared to the conventionally fabricated Zr-based BMG with the same composition (hardness ~6.0 GPa and strength ~1.5 GPa). The observed small ductility in the sample fabricated at a scan speed of 1500 mm/s was probably caused by the small dark Al-enriched phases (Fig. 5). However, further detailed investigations are needed to reveal the mechanism of how this tiny dark Al-enrich phases influence the ductility of the SLM-fabricated Zr-based BMGs.

5. Conclusion

In this study, a large scale, complex and fully dense crack-free $Zr_{52.5}Ti_5Cu_{17.9}Ni_{14.6}Al_{10}$ BMG was successfully fabricated through SLM. The influence of processing parameters on the microstructure and mechanical properties of the fabricated BMGs were systematically investigated. The following points are drawn from this study:

(1) Although higher $\overline{E_p}$ results in a higher cooling rate during SLM of BMGs, the non-uniform melt flow originating from the high laser energy deteriorates the chemical homogeneity of the melt pool.
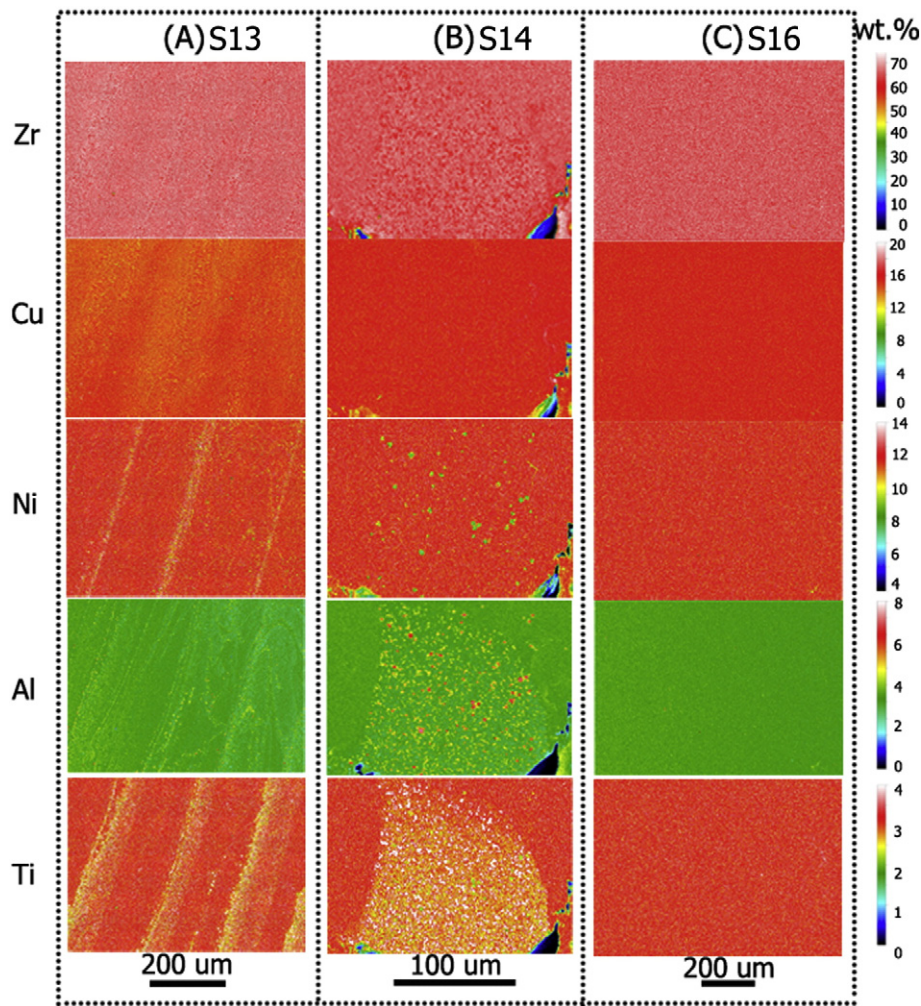
Fig. 11. Quantitative chemical maps obtained using EPMA showing the constituent elements distribution within the SLM-fabricated $Zr_{52.5}Ti_5Cu_{17.9}Ni_{14.6}Al_{10}$ BMGs using scanning strategy III at different scan speeds: (a) 500; (b) 1000 and (c) 2000 mm/s.

This results in severe crystallisation within SLM-fabricated Zr-based MG components. In contrast, a homogeneous distribution of the elements and no crystallisation can be detected at lower $\overline{E_p}$. This indicates that chemical homogeneity is the key to the successful fabrication of fully amorphous BMGs and therefore lower $\overline{E_p}$ should be used.

(2) Multiple scans resulted in a more homogenous distribution of the constituent elements within the melt pool and therefore increased the amount of the amorphous phase. The underlying reason was that the melt flow provides a force which can move the constituent elements within the melt pool. Single scan is likely to induce an unevenly distributed force which would cause elemental segregation to occur within the melt pool, which results in a very inhomogeneous and random distribution of the constituent elements. In contrast to single scan, multiple scans can result in an averaging of the melt flow and therefore a more homogenous distribution of the elements.

(3) Due the heating rate-dependent on-set crystallisation temperature of metallic glasses and the better GFA and thermal stability of the Zr-based MG, the HAZ formed from the subsequent layers does not induce crystallisation. In addition, the phase formation and microstructure of the SLM-fabricated Zr-based BMGs can be effectively tailored by varying the SLM processing parameters. As a result of the tailorable microstructure, the mechanical properties (hardness, strength and etc.) can also be controlled. This provides a promising approach to fabricate BMGs with desired properties by SLM.

References

[1] J. Eckert, J. Das, S. Pauly, C. Duhamel, Mechanical properties of bulk metallic glasses and composites, J. Mater. Res. 22 (2007) 285–301.
[2] J.F. Löffler, Bulk metallic glasses, Intermetallics 11 (2003) 529–540.
[3] C. Suryanarayana, A. Inoue, Bulk Metallic Glasses, CRC Press, 2010.
[4] W. Wang, Bulk metallic glasses with functional physical properties, Adv. Mater. 21 (2009) 4524–4544.
[5] A. Greer, E. Ma, Bulk metallic glasses: at the cutting edge of metals research, MRS Bull. 32 (2007) 611–619.
[6] A. Inoue, N. Nishiyama, New bulk metallic glasses for applications as magnetic-sensing, chemical, and structural materials, MRS Bull. 32 (2007) 651–658.

[7] A. Inoue, X. Wang, W. Zhang, Developments and applications of bulk metallic glasses, Rev. Adv. Mater. Sci. 18 (2008) 1–9.

[8] J. Schroers, G. Kumar, T.M. Hodges, S. Chan, T.R. Kyriakides, Bulk metallic glasses for biomedical applications, JOM 61 (2009) 21–29.

[9] W.H. Wang, C. Dong, C. Shek, Bulk metallic glasses, Mater. Sci. Eng. R 44 (2004) 45–89.

[10] J. Schroers, Processing of bulk metallic glass, Adv. Mater. 22 (2010) 1566–1597.

[11] H. Choi-Yim, R. Conner, F. Szuecs, W. Johnson, Processing, microstructure and properties of ductile metal particulate reinforced Zr57Nb5Al10Cu15.4Ni12.6 bulk metallic glass composites, Acta Mater. 50 (2002) 2737–2745.

[12] R. Conner, R. Dandliker, W.L. Johnson, Mechanical properties of tungsten and steel fiber reinforced Zr41.25Ti13.75Cu12.5Ni10Be22.5 metallic glass matrix composites, Acta Mater. 46 (1998) 6089–6102.

[13] D.C. Hofmann, J.-Y. Suh, A. Wiest, G. Duan, M.-L. Lind, M.D. Demetriou, W.L. Johnson, Designing metallic glass matrix composites with high toughness and tensile ductility, Nature 451 (2008) 1085–1089.

[14] F. Szuecs, C. Kim, W. Johnson, Mechanical properties of Zr56.2Ti13.8Nb5.0Cu6.9Ni5.6Be12.5 ductile phase reinforced bulk metallic glass composite, Acta Mater. 49 (2001) 1507–1513.

[15] S. Pauly, L. Löber, R. Petters, M. Stoica, S. Scudino, U. Kühn, J. Eckert, Processing metallic glasses by selective laser melting, Mater. Today 16 (2013) 37–41.

[16] H. Sun, K.M. Flores, Microstructural analysis of a laser-processed Zr-based bulk metallic glass, Metall. Mater. Trans. A 41 (2010) 1752–1757.

[17] H. Sun, K.M. Flores, Spherulitic crystallization mechanism of a Zr-based bulk metallic glass during laser processing, Intermetallics 43 (2013) 53–59.

[18] D. Gu, W. Meiners, K. Wissenbach, R. Poprawe, Laser additive manufacturing of metallic components: materials, processes and mechanisms, Int. Mater. Rev. 57 (2012) 133–164.

[19] T. Vilaro, V. Kottman-Rexerodt, M. Thomas, C. Colin, P. Bertrand, L. Thivillon, S. Abed, V. Ji, P. Aubry, P. Peyre, T. Malot, Direct fabrication of a Ti-47Al-2Cr-2Nb alloy by selective laser melting and direct metal deposition processes, Adv. Mater. Res. 89 (2010) 586.

[20] X. Li, C. Kang, H. Huang, L. Zhang, T.B. Sercombe, Selective laser melting of an Al86Ni6Y4.5Co2La1.5 metallic glass: processing, microstructure evolution and mechanical properties, Mater. Sci. Eng. A 606 (2014) 370–379.

[21] X. Li, C. Kang, H. Huang, T. Sercombe, The role of a low-energy–density re-scan in fabricating crack-free Al85Ni5Y6Co2Fe2 bulk metallic glass composites via selective laser melting, Mater. Des. 63 (2014) 407–411.

[22] X. Li, M. Roberts, Y. Liu, C. Kang, H. Huang, T. Sercombe, Effect of substrate temperature on the interface bond between support and substrate during selective laser melting of Al–Ni–Y–Co–La metallic glass, Mater. Des. 65 (2015) 1–6.

[23] A. Simchi, H. Pohl, Effects of laser sintering processing parameters on the microstructure and densification of iron powder, Mater. Sci. Eng. A 359 (2003) 119–128.

[24] V.J. Challis, X. Xu, L.C. Zhang, A.P. Roberts, J.F. Grotowski, T.B. Sercombe, High specific strength and stiffness structures produced using selective laser melting, Mater. Des. 63 (2014) 783–788.

[25] S.J. Sameehan, V.G. Anna, K. Shravana, B.D. Narendra, Dynamic crystallization during non-isothermal laser treatment of Fe–Si–B metallic glass, J. Phys. D. Appl. Phys. 48 (2015) 495501.

[26] S. Katakam, J.Y. Hwang, S. Paital, R. Banerjee, H. Vora, N.B. Dahotre, In situ laser synthesis of Fe-based amorphous matrix composite coating on structural steel, Metall. Mater. Trans. A 43 (2012) 4957–4966.

[27] C. Ma, Fundamental Study on Laser Interaction with Metal Matrix Nanocomposites, 2015.

[28] W. Liu, L. Ye, K. Liu, Micro-nano scale ripples on metallic glass induced by laser pulse, J. Appl. Phys. 109 (2011) 043109.

[29] X.P. Li, M. Yan, B.J. Yang, J.Q. Wang, G.B. Schaffer, M. Qian, Crystallization behaviour and thermal stability of two aluminium-based metallic glass powder materials, Mater. Sci. Eng. A 530 (2011) 432–439.

[30] W.L. Johnson, G. Kaltenboeck, M.D. Demetriou, J.P. Schramm, X. Liu, K. Samwer, C.P. Kim, D.C. Hofmann, Beating crystallization in glass-forming metals by millisecond heating and processing, Science 332 (2011) 828–833.

[31] Z. Lu, C. Liu, W. Porter, Role of yttrium in glass formation of Fe-based bulk metallic glasses, Appl. Phys. Lett. 83 (2003) 2581–2583.

[32] X. Li, X. Wang, M. Saunders, A. Suvorova, L. Zhang, Y. Liu, M. Fang, Z. Huang, T.B. Sercombe, A selective laser melting and solution heat treatment refined Al–12Si alloy with a controllable ultrafine eutectic microstructure and 25% tensile ductility, Acta Mater. 95 (2015) 74–82.

[33] K.N. Amato, S.M. Gaytan, L.E. Murr, E. Martinez, P.W. Shindo, J. Hernandez, S. Collins, F. Medina, Microstructures and mechanical behavior of Inconel 718 fabricated by selective laser melting, Acta Mater. 60 (2012) 2229–2239.

[34] D. Gu, Y.-C. Hagedorn, W. Meiners, G. Meng, R.J.S. Batista, K. Wissenbach, R. Poprawe, Densification behavior, microstructure evolution, and wear performance of selective laser melting processed commercially pure titanium, Acta Mater. 60 (2012) 3849–3860.

[35] L. Thijs, K. Kempen, J.-P. Kruth, J. Van Humbeeck, Fine-structured aluminium products with controllable texture by selective laser melting of pre-alloyed AlSi10Mg powder, Acta Mater. 61 (2013) 1809–1819.

[36] L. Thijs, F. Verhaeghe, T. Craeghs, J. Van Humbeeck, J.-P. Kruth, A study of the microstructural evolution during selective laser melting of Ti–6Al–4V, Acta Mater. 58 (2010) 3303–3312.

[37] X. Li, M. Yan, H. Imai, K. Kondoh, J. Wang, G. Schaffer, M. Qian, Fabrication of 10 mm diameter fully dense Al86Ni6Y4.5Co2La1.5 bulk metallic glass with high fracture strength, Mater. Sci. Eng. A 568 (2013) 155–159.

[38] S.S. Joshi, P. Samimi, I. Ghamarian, S. Katakam, P.C. Collins, N.B. Dahotre, Tensile behavior of laser treated Fe-Si-B metallic glass, J. Appl. Phys. 118 (2015) 164904.